

General Disclaimer

One or more of the Following Statements may affect this Document

- This document has been reproduced from the best copy furnished by the organizational source. It is being released in the interest of making available as much information as possible.
- This document may contain data, which exceeds the sheet parameters. It was furnished in this condition by the organizational source and is the best copy available.
- This document may contain tone-on-tone or color graphs, charts and/or pictures, which have been reproduced in black and white.
- This document is paginated as submitted by the original source.
- Portions of this document are not fully legible due to the historical nature of some of the material. However, it is the best reproduction available from the original submission.

NASA-85

(NASA-CR-174367) RESOLUTION ENHANCEMENT OF
MULTICHANNEL MICROWAVE IMAGERY FROM THE
NIMBUS-7 SMMR FOR MARITIME RAINFALL ANALYSIS
(Wisconsin Univ.) 29 p HC 203/MF A01

N85-19221

Unclas
14244

CSCI 20W G3/32

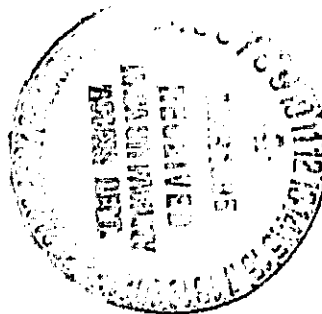
RESOLUTION ENHANCEMENT OF MULTICHANNEL MICROWAVE IMAGERY
FROM THE NIMBUS-7 SMMR FOR MARITIME RAINFALL ANALYSIS

William S. Olson^{1,2}

Chia-Lung Yeh³

James A. Weinman^{1,2}

Roland T. Chin³



¹Department of Meteorology, University of Wisconsin-Madison, Madison, WI 53706

²Space Science and Engineering Center, University of Wisconsin-Madison,
Madison, WI 53706

³Department of Electrical and Computer Engineering, University of Wisconsin-
Madison, Madison, WI 53706.

ABSTRACT:

A restoration of the 37, 21, 18, 10.7, and 6.6 GHz satellite imagery from the Scanning Multichannel Microwave Radiometer (SMMR) aboard Nimbus-7 to 22.2 km resolution is attempted using a deconvolution method based upon nonlinear programming. The images are deconvolved with and without the aid of prescribed constraints, which force the processed image to abide by partial a priori knowledge of the high-resolution result. The restored microwave imagery may be utilized to examine the distribution of precipitating liquid water in maritime rain systems.

1. INTRODUCTION

Knowledge of maritime precipitation amounts is useful in climatological energy budget studies, as well as in the diagnosis of latent heating processes in individual storms, such as tropical cyclones. In addition, remotely-sensed rainfall distributions that are retrieved in real time can be incorporated into forecast model initialization schemes.

The sensitivity of upwelling microwave brightness temperatures at the Scanning Multichannel Microwave Radiometer frequencies (37, 21, 18, 10.7, and 6/6 GHz) to variations in precipitation liquid water content of maritime clouds has been demonstrated both theoretically (Olson, et al., 1982) and by statistical correlation of measured radiances with available radar data (Spencer, et al., 1983). This sensitivity provides a means to remotely determine precipitation liquid water content in storms over the ocean, where measurements from radar or rain gauge networks are unavailable.

Due to the fixed aperture size of the SMMR, the spatial resolution of the instrument at the earth's surface diminishes in inverse proportion to the channel frequency. Thus at 37 GHz the footprint dimension is 18 km x 27 km,

compared to a maximum footprint dimension of 95 km × 148 km at 6.6 GHz. It has been demonstrated theoretically by Olson, et al. (1982) that the lower frequency SMMR channels are more sensitive to changes in cloud precipitation liquid water content than the 37 GHz channels at moderate to high rainfall rates, if all measurements are made at ideal resolution. Unfortunately, much of the information contained in the lower frequency channels is degraded due to the inadequate spatial resolution of these channels. This kind of image degradation is especially serious in coastal regions, where blurring of a bright coastal land mass can obscure rain features over the adjacent ocean.

In the present study, digital image processing techniques are applied to the SMMR imagery for the purpose of restoring all channels to a common 22.2 km resolution.

2. SOLUTION OF THE DECONVOLUTION PROBLEM

The effect of finite antenna aperture size on sensor resolution can be modeled as an antenna blurring function, \vec{H}_1 , applied to an ideal resolution image \vec{f} . The antenna blurring function is estimated in the next section for each of the SMMR channels. Given the effect of additive noise \vec{e} , the resulting low-resolution, observed image \vec{g} is expressed

$$\vec{g} = \vec{H} * \vec{f} + \vec{e} . \quad (1)$$

Here, the symbol * denotes the two-dimensional convolution operation.

The relationship (1) actually represents a system of equations governing the unknown \vec{f} in the discretely-sampled image domain. If the observed image \vec{g} is interpolated to an $I \times J$ cartesian grid, and \vec{H} is a square matrix with dimension N , then there exists for each image grid element g_{ij} a governing equation

$$g_{ij} = \sum_{k,\ell}^N H_{k\ell} f_{st} + \epsilon_{ij}, \quad (N \text{ odd}) \quad (2)$$

$$s = i - [(N-1)/2] + k - 1$$

$$t = j - [(N-1)/2] + \ell - 1$$

where the unknown \vec{f} is an $(I+N-1) \times (J+N-1)$ cartesian image grid.

Both the estimation of the antenna blurring function \vec{H} and the deconvolution of \vec{g} to estimate \vec{f} are accomplished using the nonlinear programming method described by Yeh, et al. (1984). Basically, the method considered by Yeh optimizes a given function (\vec{f} or \vec{H} in this study) by minimizing the mean-square error

$$\frac{1}{I \cdot J} \sum_{i,j}^{I,J} [\epsilon_{ij}(\vec{f}, \vec{H})]^2 = \frac{1}{I \cdot J} \sum_{i,j}^{I,J} [(\vec{H} * \vec{f})_{ij} - g_{ij}]^2 \quad (3)$$

subject to the constraining relation

$$P(\vec{f}, \vec{H}) = 0. \quad (4)$$

The function $P(\vec{f}, \vec{H})$ expresses the difference between some property of the current estimate of \vec{f} (or \vec{H}) and that of the desired result, based upon physical laws or other a priori information. Specific constraint functions employed in the estimation of the antenna blurring function and the restoration of SMMR imagery are defined in sections 3 and 4b, respectively.

A nonlinear programming method referred to as the penalty function method by Bazaraa and Shetty (1979) is utilized to solve the constrained optimization problem (Eqs. 3 and 4 above). In the penalty function approach, the constrained optimization problem is treated as a sequence of unconstrained problems. For each step of the sequence the combination

$$\psi(\vec{f}, \vec{H}, \Lambda) \equiv \frac{1}{I \cdot J} \sum_{i,j}^{I,J} [e_{ij}(\vec{f}, \vec{H})]^2 + \Lambda \cdot P(\vec{f}, \vec{H}) \quad (5)$$

is minimized using a standard technique to optimize \vec{f} (or \vec{H}). The conjugate gradient method of Fletcher and Reeves (1964), which allows faster convergence than the steepest descent method for differentiable functions such as $\psi(\vec{f}, \vec{H}, \Lambda)$, was employed to optimize \vec{f} (or \vec{H}) in this study.

In the initial step, the parameter Λ is set to a small value, such that the norm of the penalty $\Lambda \cdot P(\vec{f}, \vec{H})$ is negligibly small with respect to the norm of $\psi(\vec{f}, \vec{H}, \Lambda)$. A value of $\Lambda = 10^{-5}$ was determined to be sufficiently small for applications in this study. Since the initial weighting of the constraint function $P(\vec{f}, \vec{H})$ is relatively small, subsequent minimization of $\psi(\vec{f}, \vec{H}, \Lambda)$ using the conjugate gradient method leads to an optimal \vec{f} (or \vec{H}) which is close to the unconstrained result.

On each succeeding step the parameter Λ is increased by a factor of ten following by minimization of $\psi(\vec{f}, \vec{H}, \Lambda)$ by the conjugate gradient method. In this way, the influence of the constraint is gradually introduced.

It is demonstrated in Bazarra and Shetty (1979) that under certain general conditions the norm of the penalty $\Lambda \cdot P(\vec{f}, \vec{H})$ tends to zero as Λ tends to infinity by this procedure, and the norm of $\psi(\vec{f}, \vec{H}, \Lambda)$ meanwhile approaches a local minimum. In this study the sequence of steps was terminated with $\Lambda = 10^3$ on the last step, since it was observed, in general, that the norm of the penalty became negligibly small for this step, and the norm of $\psi(\vec{f}, \vec{H}, \Lambda)$ converged to a minimum value.

Since the image deconvolution problem is generally underdetermined (see Section 4a), it is possible that the parameter space of $\psi(\vec{f}, \vec{H}, \Lambda)$ has numerous local minima, and that the solution \vec{f} obtained by local minimization of $\psi(\vec{f}, \vec{H}, \Lambda)$ may differ from the ideal-resolution image \vec{f} . The imposition of

restrictive constraints will reduce the number of possible solutions. Also, choosing an initial guess for \vec{f} which is close to the expected solution (e.g. the original image \vec{g}), spurious solutions may be avoided.

If desired the unconstrained solution may be obtained simply by setting Λ equal to zero initially.

3. ESTIMATION OF THE ANTENNA BLURRING FUNCTION

In order to determine the antenna blurring function H , cloud-free SMMR swaths of the Florida coastline were first selected. Based upon physical models (Olson, et al., 1982) one would expect that the microwave radiances emitted from land and ocean areas to differ by at least 50 K. In addition, the absence of clouds suggests that in each region the microwave brightness should be almost spatially uniform. Only minor brightness variations would be introduced by inhomogeneities in atmospheric water vapor and, in land regions, differences in soil moisture. At ideal resolution, therefore, the land/ocean interface represents nearly a step-function discontinuity in brightness temperature. The effect of antenna blurring is to smooth this discontinuity in the observed imagery.

Using the cloud-free SMMR imagery, an approximate ideal-resolution image (f in Eq. 1) was created for each channel. The corresponding low-resolution brightness temperature data in scan format were first interpolated to a local 6° latitude \times 6° longitude cartesian grid with 22.2 km grid spacing (5 grid point per degree latitude) using the Laplacian smoothing spline fitting procedure of Wendelberger (1981). Land and ocean brightness temperatures, assumed to be spatially uniform at high resolution, were then estimated from brightness temperature values sampled far from the blurred coastline. Coastline geography from USGS survey maps and the 37 GHz imagery were utilized

to locate the land/ocean brightness discontinuity at grid resolution. An ideal-resolution brightness temperature image \vec{f} for the 37, 21, 18, 10.7 and 6.6 GHz channels in both parallel and perpendicular polarizations was estimated in this way.

Given \vec{f} and the observed image \vec{g} in each channel, Eq. (1) was solved for \vec{H} using the method of Yeh, et al. (1984), subject to the condition that \vec{H} should be normalized:

$$P(\vec{H}) = \left(\sum_{k,\ell}^N H_{k\ell} - 1 \right)^2 . \quad (6)$$

Each blurring function was defined on an $N \times N$ moveable grid, or convolution template, where the dimension N was adjusted to accommodate blurring operators of various sizes: for example, the 37 GHz channels, with a footprint size of 18 km \times 27 km, required a 5 \times 5 template (110 km \times 110 km 22.2 km grid spacing), whereas the 6.6 GHz channels required a 15 \times 15 template (330 km \times 330 km). The convolution template for each channel was made large enough to ensure that the magnitude of the blurring function outside the template boundaries was negligibly small. The template dimension was therefore chosen such that the blurring function value at the template edge was less than 10% of the central maximum value. A schematic depiction of the 37n GHz convolution template is presented in Fig. 1.

Separate blurring functions for day and nighttime SMMR overpasses were determined, since the scan line orientation relative to the image grid axes differs for ascending (daytime) and descending (nighttime) swaths. The initial guess blurring function for each channel was a Gaussian field with a dispersion width (2σ) roughly equal to the published footprint dimension (ref. Gloersen and Hardis, 1978).

In Fig. 2, the estimated blurring functions for the daytime SMMR overpass in the perpendicular polarization at 37, 18, and 6.6 GHz are presented. It should be noted that the antenna blurring functions derived here include the average effects of varying scan geometry within the swath and sensor integration time. The resulting functions are therefore smoother than those that would be expected from aperture diffraction theory (see Jackson, 1975, p. 441 ff.).

The figure dramatically illustrates the large difference in the magnitude of blurring between the highest and lowest frequency SMMR channels. Because the observed imagery results from a convolution of the ideal-resolution imagery with the blurring function for each channel, the sharply peaked 37 GHz antenna function yields observed imagery with spatial resolution only slightly worse than the grid resolution of 22.2 km. Conversely, the 6.6 GHz blurring function is nearly flat, which leads to observed imagery with relatively poor spatial resolution.

4. APPLICATION OF THE DECONVOLUTION METHOD TO SMMR IMAGERY

4a. The Model Constraint

Given the estimated blurring function \vec{H} , the system of equations which must be solved for the high-resolution image \vec{f} is necessarily underdetermined as suggested by Eq. (2). This arises from the fact that the convolution template is of finite size. The convolution by \vec{H} outside the boundaries of the observed image \vec{g} . The number of equations in the system is equal only to the number of grid elements in \vec{f} , which always has a greater dimension. This situation is illustrated in Fig. 1. The larger the blurring template \vec{H} , the larger the border region in \vec{f} , and the more degrees of freedom the system acquires.

The degrees of freedom in the system can be reduced if certain partial knowledge of the solution can be determined a priori. An analytical model for microwave brightness temperature, upwelling from a precipitation-free atmosphere over the ocean has been developed to provide such prior knowledge. The model is based upon a simplified version of the radiative transfer solution for the brightness upwelling from a plane-parallel, isothermal, absorbing atmosphere. The brightness temperature at viewing angle $\theta_0 = \cos^{-1} \mu_0$, at frequency ν and polarization p is:

$$\begin{aligned}
 TB_{\nu\rho}(U_*, \Pi_\nu, T_{sfc}) &= (1-r_{\nu\rho}) \cdot T_{xsc} \cdot \Pi_\nu & (7) \\
 &+ T_{atm_\nu} \cdot (1-\Pi_\nu) \cdot (1+r_{\nu\rho} \Omega_{\nu\rho} \Pi_\nu) \\
 &+ T_{bb} r_{\nu\rho} \Omega_{\nu\rho} \Pi_\nu^2
 \end{aligned}$$

Here, T_{sfc} is the ocean skin temperature, Π_ν is the total transmittance of the atmosphere and T_{bb} is the cosmic background radiance (2.7 K). The sea surface reflectivity $r_{\nu\rho}$ is given by the Wentz (1983) parameterization,

$$r_{\nu\rho}(T_{sfc}, U_*) = (1-e_{\nu\rho}(T_{sfc})) - M_{\nu\rho} U_* , \quad (8)$$

where $e_{\nu\rho}$, the calm sea surface emissivity, and $M_{\nu\rho}$, an empirical constant, are both given by Wentz, and U_* is the surface friction velocity. The variable $\Omega_{\nu\rho}$, parameterized

$$\Omega_{\nu\rho} = 1 + \omega_{\omega\rho} \cdot U_* \quad (9)$$

with ω_{vp} an empirical constant, is another factor provided by Wentz to account for the change in sea surface reflectivity due to wind-roughening. Finally, the effective atmospheric emission temperature T_{atm_λ} is parameterized

$$T_{atm_\lambda} = K_v \cdot T_{sfc} \quad (10)$$

The empirical constant K_v were determined by fitting the model to clear-atmosphere SMMR brightness temperature data from the Gulf of Mexico. Values of K_v , listed in Table 1, display a slight dependence on clear-atmosphere optical thickness, which is a maximum at the 22.235 GHz water vapor resonance line. The atmospheric transmittance is further decomposed as

$$\pi_v = \pi_{dr_v} \cdot \pi_{cld_v} \quad (11)$$

where π_{cld_v} is the transmittance in clear air, and

$$\pi_{cld_v} = (\pi_{cld_{37}})^{\gamma_v} \quad (12)$$

is an approximation for the transmittance through a layer of non-precipitating cloud droplets. Equation (12), with constants γ_v listed in Table 1, is based upon Rayleigh theory which accurately describes absorption by droplets with small size parameters $x = 2\pi ac/\nu$. Here, a is the droplet radius, c is the speed of light in a vacuum, and ν is the frequency of radiation. A size parameter upper limit of .02 is obtained for a non-precipitating droplet radius of 100 μm at 37 GHz. The Rayleigh criterion is therefore well satisfied.

Utilizing Eqs. (7-12), it was possible to estimate the 21, 18, 10.7, and 6.6 GHz brightness temperatures in the rain-free area of each scene at 37 GHz resolution by the following method. The SMMR images in all channels were

first gridded at 22.2 km resolution as described in the preceding section. The rain-free portion of a given scene was then determined by thresholding a histogram of the gridded $TB_{37H} - TB_{37L}$ values, which are inversely proportional to the atmospheric optical thickness. The $TB_{37H} - TB_{37L}$ distribution was found to be bimodal in all cases, with a distinct modal peak comprised of clear or nearly clear image grid elements over the ocean in addition to a broader, less well-defined peak generated by grid elements in rain regions or those over land. A double Gaussian fit to this distribution was performed. Rain-free grid elements were defined as those for which the 37 GHz polarization difference fall within one standard deviation of the "clear-air" modal peak and also those grid elements with greater $TB_{37H} - TB_{37L}$.

The observed parallel and perpendicular 37 GHz brightness temperatures and Eqs. (7-12) were next employed to determine Π_{37} and U_* for each image grid element in the rain-free area. T_{sfc} , the only other unknown in these formulae, was derived from auxiliary ocean buoy data. In an operational framework, T_{sfc} might be approximated by the climatic mean temperature or estimated from satellite infra-red measurements. The inversion of Π_{37} and U_* was performed numerically using Newton's method in two dimensions.

Image grid elements in the rain-free area which contained the maximum values of Π_{37} were assumed to be cloud-free. Given U_* for these elements and observed brightness temperatures in the other SMMR channels, estimates of Π_{clr_v} were made using Eqs. (7-12). Although it may be argued that antenna blurring alters the brightness temperatures in the lower frequency channels, the clear-air transmittances locally calibrated in this manner were found to be more accurate than those derived from empirical relationships.

Having determined Π_{37} and Π_{clr_v} for a given image, Π_v could be computed for any grid element in the rain-free area using the inverted value Π_{37} and

Eqs. (11) and (12). The 21, 18, 10.7, and 6.6 GHz brightness temperature at 37 GHz resolution were then generated using π_v , U_* , and Eq. (7) in the rain-free region.

The method so described is essentially an extrapolation procedure, where variations in microwave brightness are mainly attributed to variations in non-precipitating cloud amount. In Section 4b, the 37 GHz resolution data is utilized to constrain the image deconvolution system.

It should be noted that although the histogram method, described above, discriminates reasonably well between grid elements in raining and rain-free regions, some misclassification of grid elements does occur. To illustrate this point, histograms of grid elements in both raining and rain-free regions over the Gulf of Mexico and Florida coast at 0540Z, 7/17/79 are presented in Fig. 3. Rain areas were identified using gridded WSR-57 radar data from the station at Apalachicola, Florida. Details of the radar gridding procedure are discussed in Section 4. The single standard deviation threshold is indicated by the vertical line at the 37 GHz polarization value of 54.1 K.

The single standard deviation threshold was designed to produce a fairly conservative constraint. If this threshold is used then the constraint model is applied to grid elements which are almost certainly rain-free, despite some misclassification of rain-free grid elements. Nevertheless, grid elements in rain regions are sometimes classified as rain-free, as it is illustrated in the figure. This latter type of misclassification is more serious because the constraint model was formulated under the assumption of a rain-free atmosphere, and might otherwise produce erroneous constraint brightness temperatures. In the future, correct classification of grid elements could be achieved using additional high resolution satellite data, such as that provided by visible and infra-red sensors.

4b. Restoration of SMMR Imagery

Eleven $6^\circ \times 6^\circ$ test areas over the Gulf of Mexico and eastern Florida coasts were chosen to evaluate the image restoration method. The areas selected (a) contained significant maritime rainfall, (b) were located within range of operational WSR-57 coastal radar, and (c) were located within the swath boundaries of the Nimbus-7 SMMR during overpasses in 1979. The brightness temperature data, in scan format, were first interpolated to latitude/longitude cartesian grids at 22.2 km spacing as described in Section 3.

Based upon the observed imagery and estimated antenna blurring function, Eq. (1) was solved for the high-resolution image f in each channel, using nonlinear programming method described by Yeh, et al. (1984). The model constraint, presented in Section 4a, was incorporated into the constraint functions $P(\vec{f})$,

$$P(\vec{f}) = \sum_{i,j} (f_{ij} - TB_{ij})^2 \quad (13)$$

summation over rain-free area

where TB_{ij} is the model-generated brightness temperature.

Two variations of the restoration method were considered. In Case A, the restored image solution was left unconstrained ($\lambda=0$), and was initialized using the observed image throughout the domain of \vec{g} . Thus no prior knowledge of the solution was utilized in Case A. Case B restorations were fully constrained in the rain-free portion of the image by allowing λ in Eq. (5) to increase in steps as the iteration proceeded. The initial guess in this case was the observed low-resolution image except in the rain-free portion, where the model constraint was imposed. In both Case A and Case B the initial guess was extended to the border region of \vec{f} by repeating the edge grid

elements in the domain of \vec{g} outward. Note that since the model constraint was derived from the 37 GHz data to be applied only to the other SMMR channels, Case B was omitted for the 37 GHz imagery.

Examples of restored imagery from the two deconvolution cases are presented in Fig. 4, where the original imagery has been included for comparison. The scene in the figure covers nearly the full extent of Hurricane David at 1644Z on 9/3/79, as it made its landfall on the eastern Florida coast at out 90 km south of Daytona Beach.

Despite the underdetermined nature of the governing system (Eq. 2), satisfactory results were obtained at 37, 21, 18, and even 10.7 GHz when the system was left unconstrained (Case A). The missing features and artifacts evident in the Case B restorations can mainly be attributed to error in the spatial constraint, arising from both misclassification of "rain-free" image elements and from error in the constraint brightness temperatures themselves.

Other types of constraints on the restored-resolution satellite imagery were considered by the authors. These included imposed maximum and minimum bounds on brightness temperature, a constraint on the total image brightness to remain constant, and constraints on the intra- and inter-channel grid element brightness temperature cross products. The latter constraints were specifically designed to preserve the mean auto- and cross-correlation statistics of the grid element brightness levels. Unfortunately, none of these constraints resulted in significant improvement of the restored image quality. It should be noted that minimization of $\psi(\vec{f}, \vec{H}, \Lambda)$ (Eq. 3) results in preservation of the expected value of the grid element brightness temperatures.

5. COMPARISON OF RESTORED MICROWAVE IMAGERY WITH WSR-57 RADAR

For each of the eleven gridded SMMR scenes a digitized radar map in the same grid projection was produced. Radar contours from coastal WSR-57 radar were transferred to a grid overlay, where each 22.2 km grid box of the overlay was centered on a corresponding SMMR image gridpoint. A mean rainfall rate, as specified in the WSR Handbook (NOAA, 1979), was assigned to the entire area covered by each radar contour level. The fractional area covered by that contour level within each 22.2 km grid box was determined using a computer-linked digitizing tablet, which allowed the computation of an area-averaged rainfall rate for each grid box (and each corresponding SMMR gridpoint). WSR-57 radar from the Daytona Beach station covering a portion of Hurricane David is included in Fig. 4 for comparison with the SMMR imagery.

Referring to Fig. 4, it may be generally noted that the quality of the restored images tends to decline with decreasing channel frequency. This trend is a consequence of the dramatic decrease in resolution of the original SMMR imagery with decreasing frequency. At 10.7 and 6.6 GHz the Case A restoration method tends to overenhance large, bright features while adjacent, less intense regions are underenhanced. This effect is especially pronounced in the Case A 6.6 GHz restoration in the vicinity of the Florida coastline, where the bright land mass is abutted by severely underenhanced rainbands. Degradation with decreasing channel frequency is also observed in the Case B imagery. In Case B the structure of the rain patterns (at 37 GHz resolution) is maintained through the influence of the spatial constraint; however, the brightness temperature values at 6.6 GHz show only modest consistency with either the radar traces or the imagery in the higher-frequency SMMR channels.

The poor quality of the 6.6 GHz restorations can be generally attributed to the large number of degrees of freedom in the governing system of equation

(Eq. 2). This problem was previously discussed in Section 4a. At 6.6 GHz there are a large number of degrees of freedom and therefore many possible solutions. The restoration procedure iterates to the solution which is closest to the initial guess. Since the initial guess field (the original blurred image) is quite smooth in Case A, only the large-scale image features are enhanced in the final solution. Incorporation of the model constraint brightness temperatures in the initial guess of the unconstrained image deconvolution did not improve the restored image quality.

The observed large-scale pattern or over-undershadowing was reproduced in the restoration of synthetic images when the size of the blurring function template was not small with respect to the image size. The SMMR swath dimensions limited the image size to a $6^\circ \times 6^\circ$ grid domain in the present study. The simulations also demonstrated that the imposition of accurate constraints helped to improve restored image quality. Unfortunately, the model constraint of Case B has limited accuracy. Instrument noise or calibration errors in the 37 GHz data can propagate through the constraint model, producing error in the constraint brightness temperatures at the lower frequencies.

Despite some degradation with decreasing frequency, the restorations at 37, 21, 18, and even 10.7 GHz show significant improvement in resolution over the original imagery. Moreover, there is reasonable consistency between channels in the position and intensity of enhanced-resolution features. The positions of radar-defined rainbands are well correlated with bright bands in these rain-sensitive microwave channels.

The restoration of Hurricane David also shows small inter-channel differences which might aid in the retrieval of maritime rainfall rates. The theory of microwave radiative transfer through extensive precipitating clouds over the

ocean indicates little change in the observed 37 GHz brightness temperature in response to changes in rainfall rate at rainfall rates greater than roughly 10 mm/hr (Olson, et al., 1982). Models also indicate increasing brightness temperature sensitivity to rainfall rate as the channel frequency decreases. Indeed, evidence of increasing rain sensitivity with decreasing channel frequency is seen in the restored imagery. Hurricane eye and rainband structure which is not obvious at 37 GHz is revealed at 21, 18, and 10.7 GHz.

A second example was selected to demonstrate the performance of the restoration procedure in the vicinity of a bright land mass. For this example, WSR-57 radar and original/restored SMMR imagery of squall line off the coast of the Florida panhandle at 1706Z, 7/11/79 are presented in Fig. 5. The restored SMMR images on the right-hand side of the figure were produced using the Case A (unconstrained) and Case B (constrained) enhancement methods.

Although the squall line is evident in the Apalachicola radar imagery, blurring of the adjacent Florida coastal region tends to obscure this feature in the original 21, 18, 10.7 and 6.6 GHz SMMR data. The problem of signal contamination in the vicinity of land masses has contributed to omission of such near-coast SMMR data in other studies (Milman, 1983; Wilhelm, et al., 1984). As seen in Fig. 5, the Case A restoration procedure both enhances the squall line and distinguishes it from coastal Florida at 37, 21, and 18 GHz. Blurring of the bright land mass at 10.7 and 6.6 GHz is so great that application of the restoration procedure does not help to delineate coastal rain features in the Case A imagery. Application of the model constraint in Case B helps to outline rain features at 10.7 and 6.6 GHz, but the brightness temperature values in the rain regions, as noted in the preceding example, are somewhat suspect.

6. CONCLUDING REMARKS

The nonlinear programming method of Yeh, et al. (1984) performed satisfactorily when applied to the restoration of 37, 21 and 18 GHz SMMR images. Utilization of a physically-based constraint helped to delineate rain features in restored 10.7 and 6.6 GHz imagery, but in general the restoration of imagery at these frequencies was difficult, owing primarily to the extremely low resolution of the original imagery and the large number of degrees of freedom in the image deconvolution problem.

Constraint effectiveness could be increased if visible, infra-red, or other high resolution satellite data were incorporated into the constraint area classification scheme. The additional information provided by these sensor data could be used to reduce the number of misclassified grid elements in the constraint. The accuracy of a constraint based upon the inversion of satellite data, such as the one developed in this study, would also benefit from future efforts to reduce instrument noise/calibration error. Another related subject under current investigation by C.-L. Yeh is the derivation of an optimal constraint weighting factor λ , which would vary as a function of the related levels of noise in the original image and the constraint.

The quality of the restored imagery might also be improved if the antenna blurring functions were more accurately estimated. In the present study only a limited amount of imagery was used to make blurring function estimates. Several coastal swaths in regions where the land portion contains nearly homogeneous, dry terrain would be required for accurate estimates. In addition a swath-oriented gridding scheme, rather than the latitude/longitude grid employed in this study, would help ameliorate the restoration procedure. Blurring functions determined in such a grid system would be independent of satellite orbital position.

The restoration method presented here may also be applied to other types of meteorological satellite imagery. Prerequisites for application are (a) the data must be interpolated, if necessary, to a regular grid, and (b) an estimate of the antenna blurring function must be made in that particular grid coordinate system. As it was demonstrated in Section 3, the antenna blurring function can be determined using the same nonlinear programming method that is utilized to enhance image resolution. In this case one must obtain a subset of images for which the ideal-resolution versions can be estimated. This approach is especially suited to imagery from multi-resolution sensors such as the SMMR or the forthcoming Mission Sensor Microwave Imager (SSM/I), since all channels are co-navigated, and there are strong correlations between features in different channels.

ACKNOWLEDGMENTS

The authors wish to acknowledge Per Gloersen and William Abbott for their efforts in supplying SMMR data in scan format. Discussions with Andrew Milmar regarding aspects of the SMMR brightness temperature calibration were also very helpful. We would also like to especially thank Roy Spencer for his guidance in the digitization of WSR-57 radar, and David Santek for his help with the SMMR navigation.

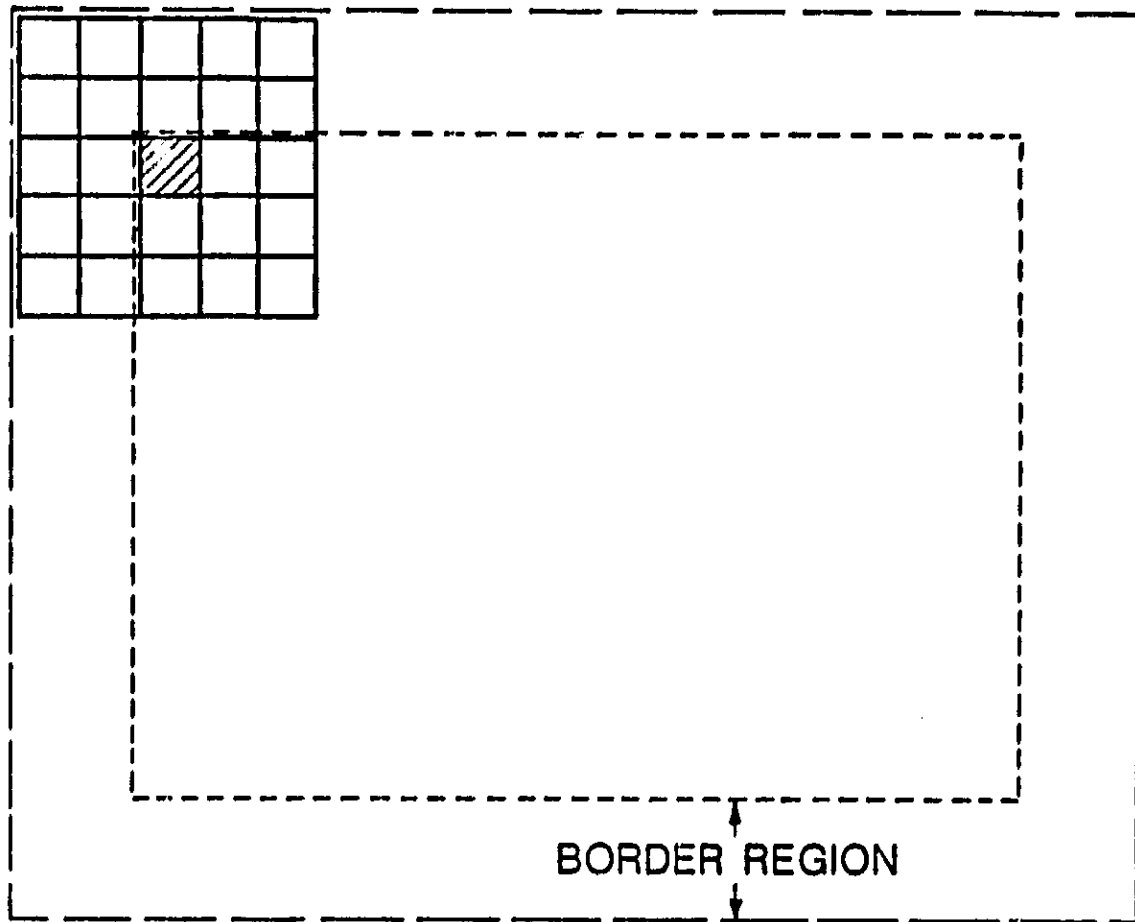
BIBLIOGRAPHY

- Bazaraa, M. S. and C. M. Shetty, 1979: Nonlinear Programming--Theory and Algorithms, John Wiley and Sons, 560 pp.
- Fletcher, R. and C. M. Reeves, 1964: Function Minimization by Conjugate Gradients, Computer Journal, 7, 149-154.
- Gloersen, P. and L. Hardis, 1978: The Scanning Multichannel Microwave Radiometer (SMMR) Experiment, The Nimbus 7 Users' Guide, jGoddard Space Flight Center, Greenbelt, MD., 263 pp.
- Jacoby, S. L. S., J. S. Kowalik and J. T. Pizzo, 1972: Iterative Methods for Nonlinear Optimization Problems, Prentice-Hall, Inc., 274 pp.
- Jackson, J. D., 1975: Classical Electrodynamics, John Wiley and Sons, 848 pp.
- Lo, R. C., 1983: A Comprehensive Description of the Mission Sensor Microwave Imager (SSM/I) Environmental Parameter Extraction Algorithm. NRL Memorandum Report 5199. Naval Research Laboratory, Washington, D.C. 48 pp.
- NOAA, 1979: Introduction to Weather Radar, U.S. Department of Commerce, 23 pp.
- Olson, W. S., J. A. Veinman and H. M. Wolf, 1982: Estimation of Rainfall Rates in Tropical Cyclones by Passive Microwave Radiometry. A Summary Report to the National Oceanic and Atmospheric Administration under Grant N. NA78-SAC-0432, 48 pp.
- Spencer, R. W., B. B. Hinton and W. S. Olson, 1983: Nimbus-7 37 GHz Radiances Correlated with Radar Rain Rates over the Gulf of Mexico, Journal of Climate and Applied Meteorology, 22, 2095-2099.
- Wendelberger, J. G., 1981: The Computation of Laplacian Smoothing Splines with Examples, Department of Statistics Technical Report No. 648, University of Wisconsin-Madison, Madison, WI 53706.

- Wentz, F. J., 1983: A Model Function for Oceanic Microwave Brightness Temperatures, Journal of Geophysical Research, 88, 1892-1908.
- Wilheit, T. T. Jr., J. R. Greaves, J. A. Gatlin, D. Han, B. M. Krupp, A. S. Milman and E. S. Chang, 1984: Retrieval of Oceanic Surface Parameters from the Scanning Multifrequency Microwave Radiometer (SMMR) on the Nimbus-7 Satellite, IEEE Transactions on Geoscience and Remote Sensing, GE-22, 133-142.
- Yeh, C.-L and R. T. Chin, 1984: Image Restoration by Nonlinear Programming Constrained Deconvolution, (in preparation).

Table 1. Empirical coefficients K_ν and exponents γ_ν used in Eqs. 10 and 12, respectively. The constants γ_ν were derived from Rayleigh theory, assuming a homogeneous, isothermal cloud layer at 273.15 K.

ν [GHZ]	K_ν	γ_ν
37	.942	1.00
21	.951	3.47×10^{-1}
18	.950	2.57×10^{-1}
10.7	.931	9.25×10^{-2}
6.6	.918	3.57×10^{-2}



----- BOUNDARY OF OBSERVED IMAGE g^v

———— BOUNDARY OF RESTORED IMAGE f^v


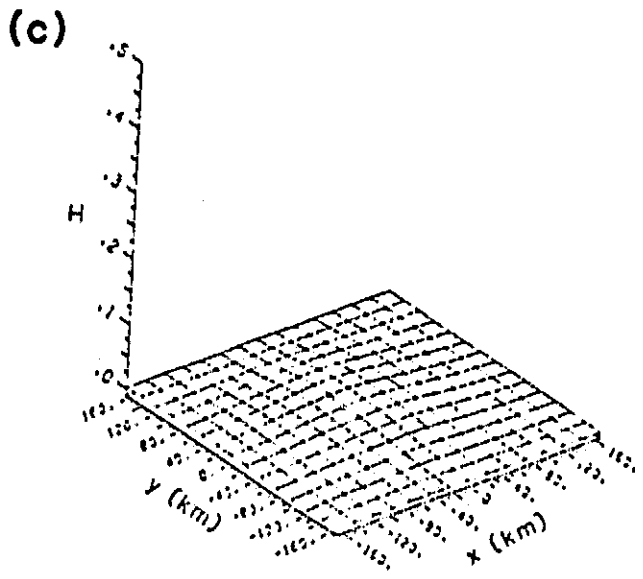
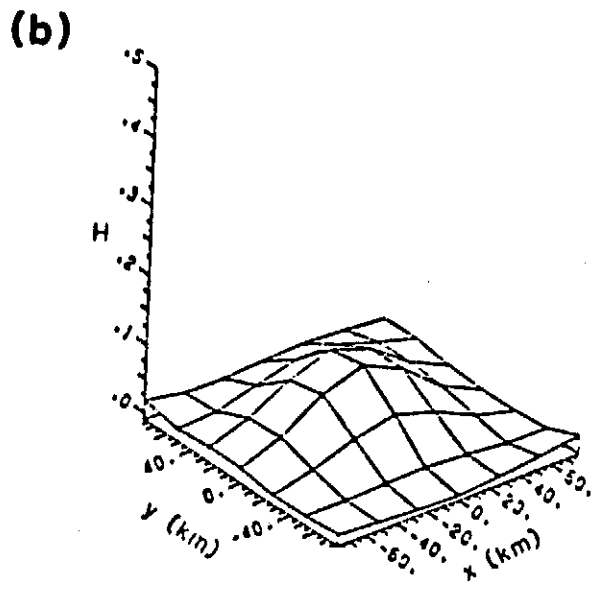
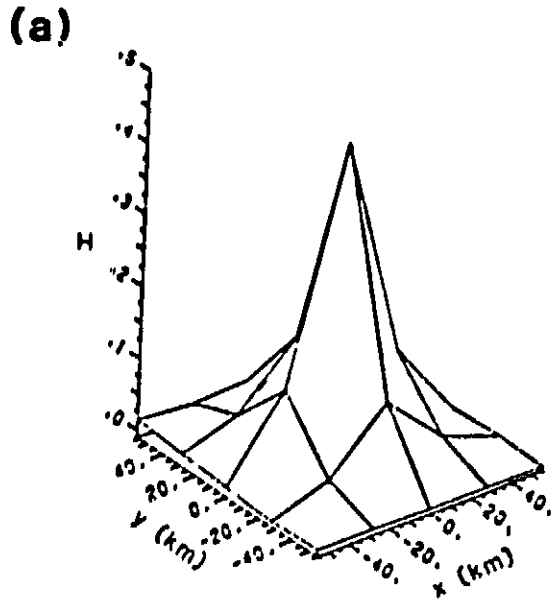

 ANTENNA BLURRING FUNCTION TEMPLATE (5x5 IN THIS EXAMPLE). THE CONVOLUTION RESULT FOR THE TEMPLATE IN THIS POSITION IS THE OBSERVED IMAGE GRID ELEMENT g_{11} , SHADED.

Fig. 1. Schematic for grid domains in the image deconvolution problem.

Fig. 2. Nimbus-7 SMMR ascending pass antenna blurring functions for the (a) 37 GHz I, (b) 18 GHz I, and (c) 6.6 GHz I channels. Horizontal displacements are measured from the convolution template center in km.



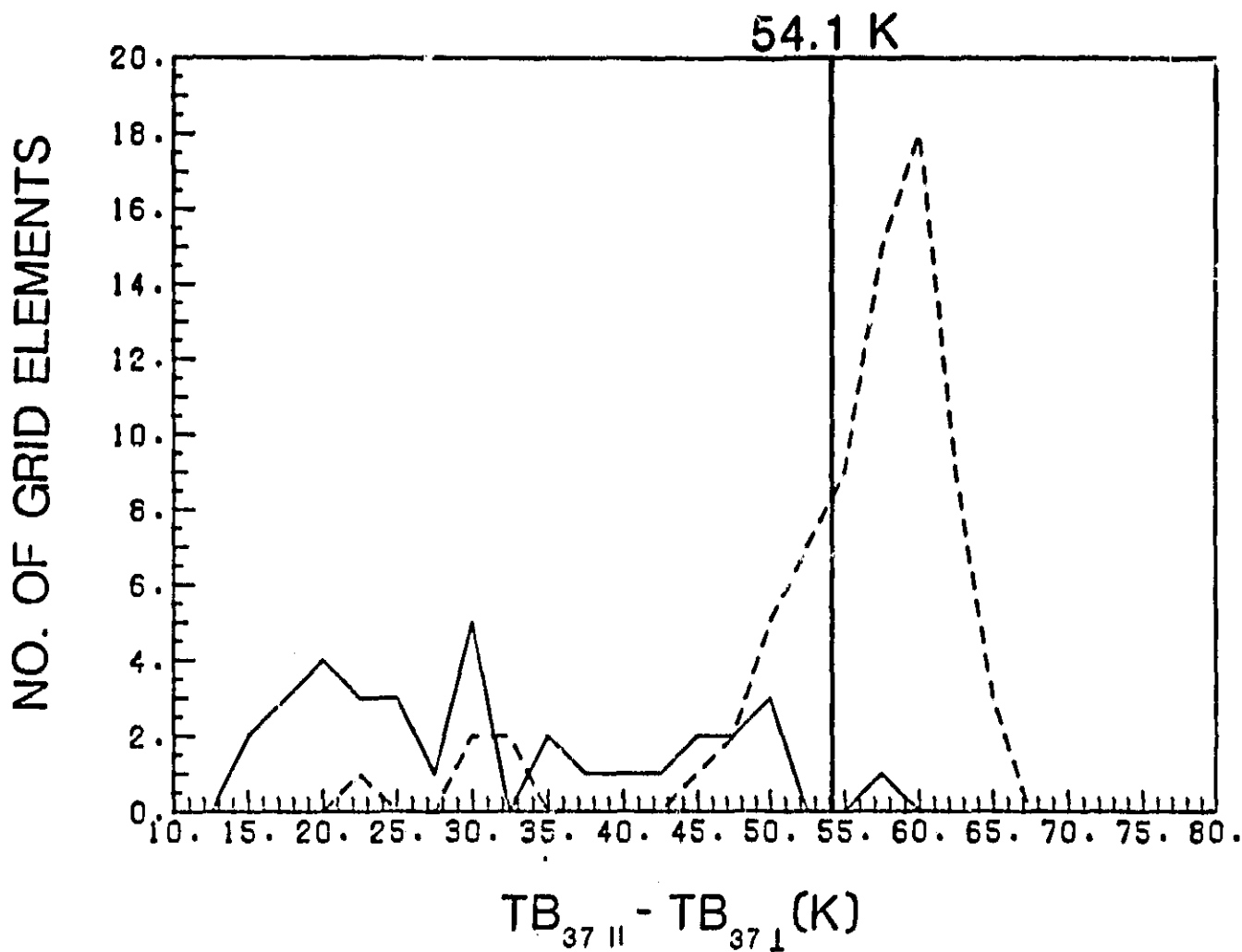


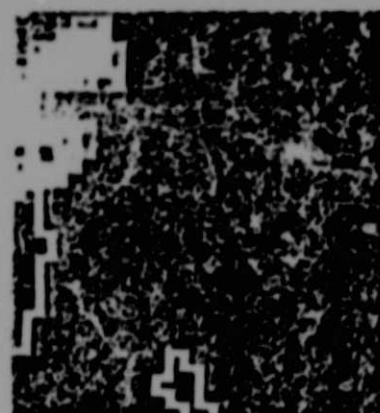
Fig. 3. Histograms of SMMR image grid elements in raining (solid line) and rain-free (dashed line) regions over the Gulf of Mexico at 0540Z, 7/17/79. Rain data were derived from the WSR-57 radar at Apalachicola, Florida. According to the classification method utilized in this study, grid elements for which the 37 GHz polarization difference is greater than the single standard deviation threshold (54.1 K) are assumed to be rain-free.



37 GHz I Original



37 GHz I Case A



WSR-57 Radar



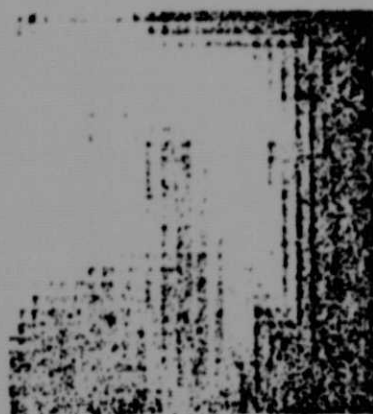
21 GHz I Original



21 GHz I Case A



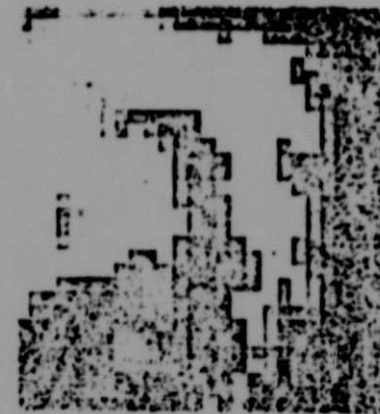
21 GHz I Case B



18 GHz I Original



18 GHz I Case A



18 GHz I Case B

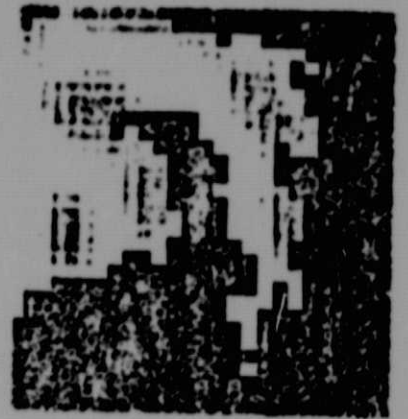
Fig. 4. WSR-57 radar, original and restored SMTR imagery of Hurricane David off the eastern Florida coast at 1644Z, 9/3/79. Case A is unconstrained; Case B is constrained.



10.7 GHz I Original



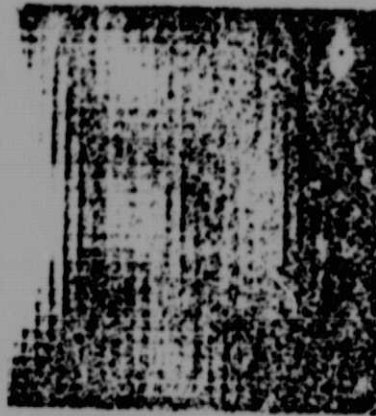
10.7 GHz I Case A



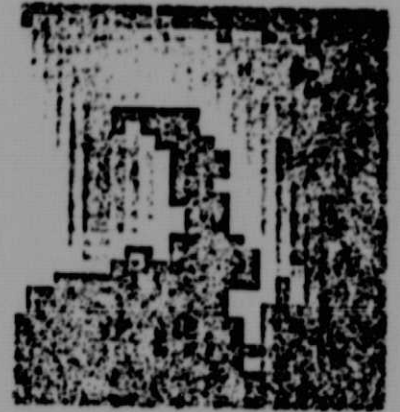
10.7 GHz I Case B



6.6 GHz I Original



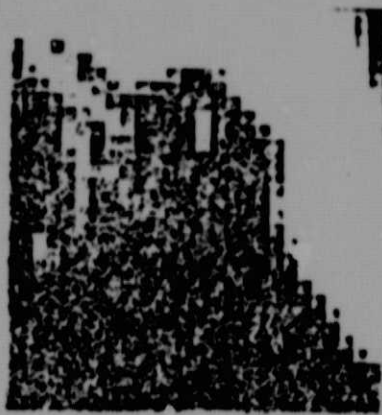
6.6 GHz I Case A



6.6 GHz I Case B

Fig. 4. (continued)

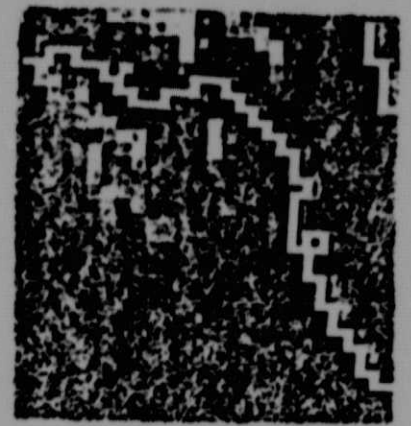
ORIGINAL PAGE
BLACK AND WHITE PHOTOGRAPH



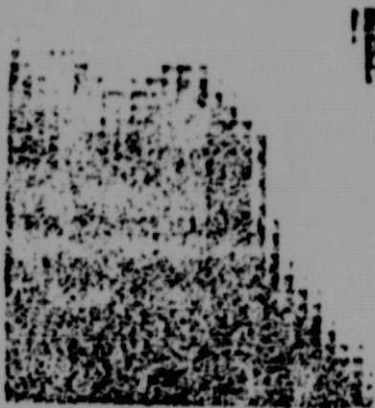
37 GHz I Original



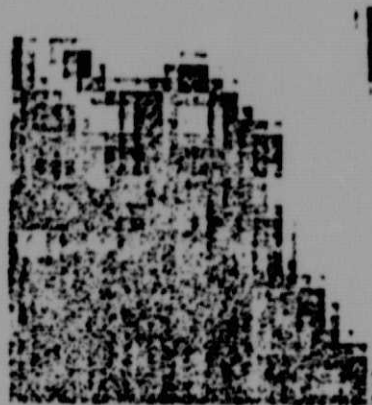
37 GHz I Case A



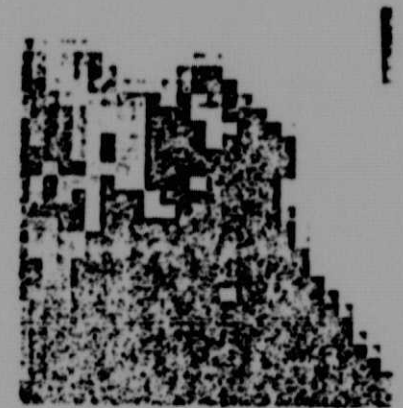
WSR-57 Radar



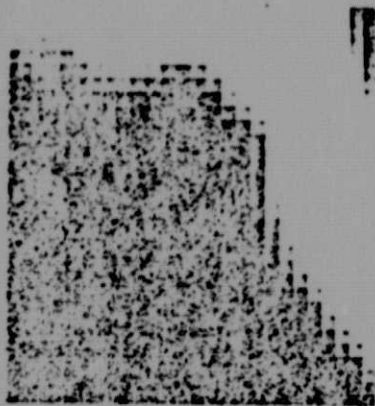
21 GHz I Original



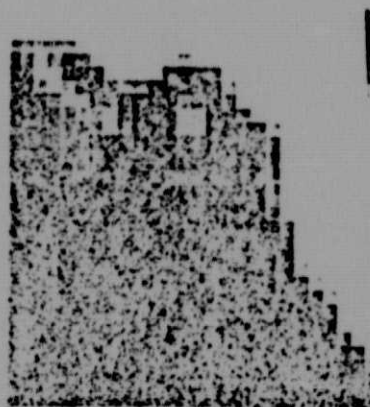
21 GHz I Case A



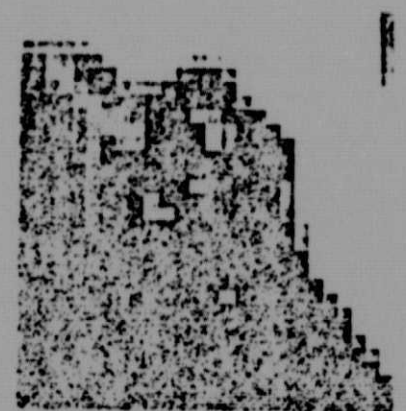
21 GHz I Case B



18 GHz I Original



18 GHz I Case A



18 GHz I Case B

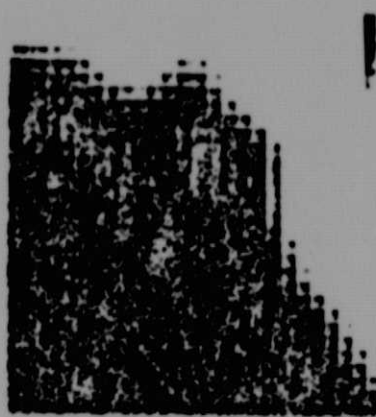
Fig. 5. WSR-57 radar, original and restored SMMR imagery of a squall line near Apalachicola, Florida at 1706Z, 7/11/79. Case A is unconstrained; Case B is constrained.

ORIGINAL PAGE

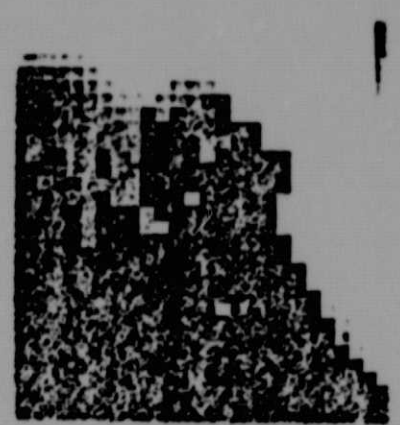
BLACK AND WHITE PHOTOGRAPH



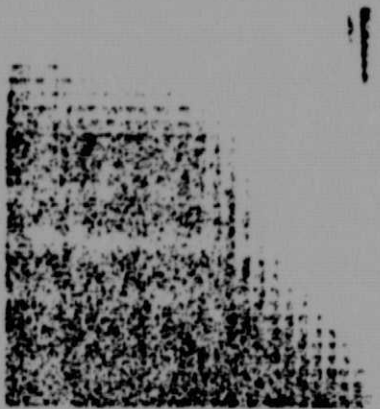
10.7 GHz I Original



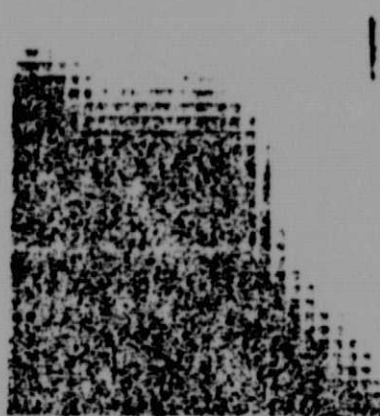
10.7 GHz I Case A



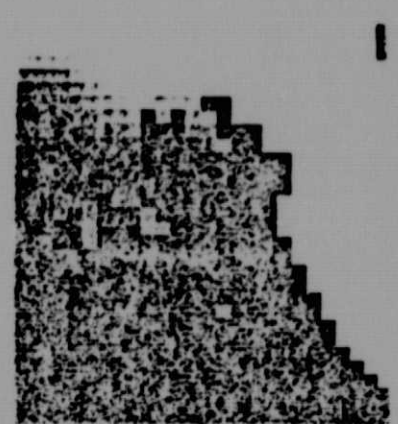
10.7 GHz I Case B



6.6 GHz I Original



6.6 GHz I Case A



6.6 GHz I Case B

Fig. 5. (continued)

ORIGINAL PAGE
BLACK AND WHITE PHOTOGRAPH